"Sol-gel auto combustion synthesis of Al^{3+}-Gd^{3+} ions co-doped cobalt ferrite nanoparticles for nanoelectronics applications"

Vaibhav K. Raut[1] · Sandeep B. Somvanshi[2] · Elmuez A. Dawi[3] · Chandrakant T. Birajdar[1]

Abstract

This study focused on investigating cobalt ferrite nanoparticles doped with trivalent Al^{3+} and Gd^{3+} ions across compositions ranging from $CoFe_{2-2x}Al_xGd_xO_4$ (x = 0.00, 0.02, 0.04, 0.06, 0.08). The nanoparticles were synthesized using the sol-gel auto-ignition method with citric acid as a chelating agent. Structural analysis via Rietveld-refined X-ray diffraction confirmed the formation of single-phase nanoparticles with a cubic spinel structure. Morphological examination through scanning electron microscopy revealed spherical-shaped grains. Elemental analysis using energy-dispersive X-ray analysis indicated consistent composition and high purity. Infrared spectra analysis verified the presence of characteristic modes typical of spinel ferrite structures. Magnetic properties assessed by vibrating sample magnetometry demonstrated soft magnetic behavior with lower coercivity. DC electrical resistivity measurements indicated a decrease in resistivity with increasing Al^{3+}-Gd^{3+} co-doping, while dielectric studies showed enhanced properties in this regard. Overall, the findings suggest that these co-doped cobalt ferrite nanoparticles hold promise for applications in magneto-electronic devices.

Graphical Abstract
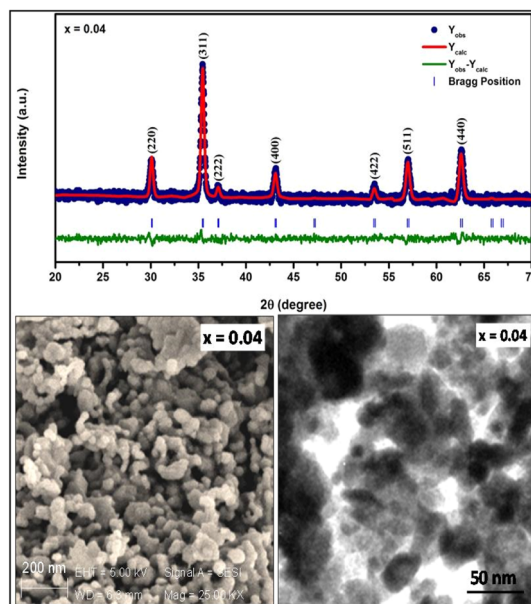
✉ Sandeep B. Somvanshi
   sbsomvanshi1993@gmail.com

✉ Chandrakant T. Birajdar
   drctbirajdar@gmail.com

[1] Department of Physics, Shri Madhavrao Patil Mahavidyalaya, Murum, Omerga, Osmanabad 413605, India

[2] School of Materials Engineering, Purdue University, West Lafayette, IN 47907, USA

[3] College of Humanities and Sciences, Ajman University, Ajman 346, United Arab Emirates

Highlights

- $CoFe_2O_4$ nanoparticles co-doped with Al^{3+} and Gd^{3+} were synthesized using sol-gel auto-combustion.
- SEM revealed spherical nanoscale grains, and XRD showed increased lattice constants with co-doping.
- Saturation magnetization and magneton number decreased with higher co-doping levels.
- Co-doping improved electrical conductivity and showed typical frequency-dependent dielectric behavior.
- These nanoparticles are promising for magneto-electronic and high-frequency applications.

1 Introduction

In the last two decades, nanomaterials and nanotechnology have been revolutionizing across various areas, offering innovative solutions and capabilities [1–3]. These advances demonstrate the wide-range impacts of nanotechnology across the different sectors, promising further breakthroughs in the future [4–6]. Nanomaterials have transformed energy and electronics sectors, offering significant improvements in performances, effectiveness, and functional ability [7–9]. While nanomaterials offer promising advantages, challenges such as scalability, cost-effectiveness, and environmental impact remain [10–12]. Recent developments in magnetic nanomaterials (MNPs) have concentrated on improving their functional abilities, showcasing their versatile nature and potentiality in numerous areas [13–15]. These advancements highlight ongoing endeavors to expand their capabilities for practical applications in areas such as health sectors, environmental issues, and energy-related applications [16–18].

Ferrite nanoparticles (FNPs) are a unique type of MNPs that are composed of iron oxide in combination with other metallic elements [19]. FNPs exhibit distinctive magnetic features due to their smaller size, typically ranging from 1–100 nm [20, 21]. FNPs are utilized across different areas, which consist of biomedical and electronic sectors [22–24]. In the biomedical field, FNPs have applications in drug delivery, magnetic hyperthermia, and as carriers for drugs that can be activated by an inductive field to target and eliminate cancer cells [25]. They are also employed as contrasting agents in magnetic resonance imaging (MRI). In electronic sectors, FNPs are employed in data storage, sensor, and for shielding against 'electromagnetic interference' [26]. Their small size and large surface area make FNPs particularly appropriate for nanoelectronics applications [19, 27].

Spinel ferrites (SFs), characterized by the notation $M^{2+}Fe^{3+}_2O_4$, where M^{2+} represents common divalent metal ions, demonstrate exceptional magnetic and electronic features due to their nanoscale size compared to bulk ferrites [28, 29]. These properties can be tailored for specific applicability through adjustments in particle size, composition, and synthesis methods [30]. Nanoscale spinel ferrites are typically synthesized using techniques such as chemical precipitation, sol-gel processes, hydrothermal reactions, and thermal decomposition of precursors [22, 31, 32]. By manipulating synthesis conditions, sizes, shapes, and magnetic characteristics of SFs nanoparticles can be optimized to create nanomaterials with tailored properties suitable for diverse applications [33].

Cobalt ferrite ($CoFe_2O_4$) nanoparticles (NPs) belong to the spinel ferrite family, characterized by a crystal structure comprising cobalt (II) oxide (CoO) and iron (III) oxide (Fe_2O_3) [34]. These nanoparticles exhibit intriguing magnetic and physical properties that make them highly versatile [23, 35]. Doped cobalt ferrite nanoparticles involve intentionally introducing dopant into the crystal lattice of $CoFe_2O_4$ [36–38]. This doping alters various features of the SFs, including 'magnetic, electrical, optical, and catalytic' characteristics [39–41]. The preparation of doped $CoFe_2O_4$ NPs follows a similar procedure as those for pristine $CoFe_2O_4$, with a dopant precursor being added during the preparation process. The precise controlling of dopant concentrations and allocation within the crystal lattice is crucial for fine-tuning the features of these nanoparticles to suit specific application. This capability to modify and optimize their properties underscores the potential of doped cobalt ferrite nanoparticles across a wide range of technological and industrial uses.

Co-doped cobalt ferrite nanoparticles represent a specialized category where $CoFe_2O_4$ NPs are altered by the incorporation of multiple types of dopants in their 'crystal lattice' during synthesis [42, 43]. This co-doping strategy allows for the manipulation and enhancement of various properties, leveraging the synergistic effects of different dopants. Typically, co-doped $CoFe_2O_4$ NPs include combinations of transition metal ions like nickel (Ni), manganese (Mn), zinc (Zn), and copper (Cu), as well as rare earth ions. The incorporation of these dopants, whether divalent or trivalent, such as aluminum (Al^{3+}), chromium (Cr^{3+}), and gadolinium (Gd^{3+}), among others, can significantly alter the characteristics of $CoFe_2O_4$ NPs. The selection and amount of dopants are crucial parameters that can be precisely controlled to tailor the properties of the nanoparticles

for specific applications. This fine-tuning capability enables researchers to optimize parameters such as magnetic behavior, electrical conductivity, optical properties, and catalytic activity, thereby expanding the potential applications of co-doped $CoFe_2O_4$ NPs in various fields of technology and industry.

In the literature, numerous studies have explored the enhanced properties of trivalent ion-doped $CoFe_2O_4$ nanoparticles across various applications. Kamran et al. [44] focused on trivalent cerium doping in cobalt ferrite nanoparticles, revealing enhanced transport properties relevant to resistive RAM applications. Rather et al. [45] reported on the physical and chemical properties of aluminum-doped mixed cobalt ferrite nanoparticles. Jing et al. [46] explored the structure and magnetic properties of $CoFe_2O_4$ NPs doped with various rare earth elements, examining the effects of different dopant positions. Despite extensive research on 'trivalent ion' co-doped ferrites, studies specifically on Al^{3+}-Gd^{3+} co-doped $CoFe_2O_4$ NPs are not often reported in current literature. This gap suggests a potential area for future research to explore the combined effects of these particular dopant on the properties and applications of $CoFe_2O_4$ NPs. Such studies could further advance our understanding and utilization of these materials in diverse technological areas.

In this work, we present a series of $CoFe_2O_4$ nanoparticles co-doped with Al^{3+} and Gd^{3+} ions, formulated as $CoFe_{2-2x}Al_xGd_xO_4$, synthesized using the sol-gel auto-ignition technique. We comprehensively investigated the different properties of these nanoparticles through rigorous characterization methods. Our findings are expected to offer important insights into the properties and prospective application of these co-doped nanoparticles. By systematically analyzing their structural integrity, infrared absorption spectra, surface characteristics, magnetic behavior, and electrical properties, we aim to establish a solid foundation for their effective utilization in practical applications. It is anticipated that the outcomes of this work will contribute to advancing the understanding and optimizing the performance of $CoFe_2O_4$ nanoparticles co-doped with Al^{3+} and Gd^{3+}. This knowledge could potentially pave the way for their enhanced application in various real-world scenarios, ranging from electronics and magnetic storage to biomedical and environmental technologies.

2 Experimental

The metal ion source materials for Co^{2+}, Fe^{3+}, Al^{3+}, and Gd^{3+} in the form of nitrate, citric acid ($C_6H_8O_7$), ammonia solution (NH_3), and deionized water employed as precursor materials were obtained from Sigma Aldrich and were used without further purification. The sol-gel auto-ignition synthesis technique was employed to synthesize $CoFe_{2-2x}Al_xGd_xO_4$ NPs. All the nitrates in proper proportion were initially dissolved in deionized water and then mixed thoroughly. Citric acid was utilized as the fuel and was mixed with the nitrate precursors solution to achieve a mole ratio of 3:1 (citric acid : metal cations). The pH of the solution was then set to ~7 by adding ammonia solution dropwise. The temperature of the pH-adjusted solution was increased gradually from 60 °C to 90 °C and then to 115 °C. Initially, a sol (solution) was obtained which was gradually converted into a gel. The temperature was further raised to 120 °C, causing the gel to auto-ignite and transform into a fine powdered state. The loose powder obtained was further grounded and sintered at 600 °C for 6 h to remove any remaining moisture and organic residues from the sample. This synthesis approach ensured the production of $CoFe_{2-2x}Al_xGd_xO_4$ nanoparticles in a controlled manner, suitable for subsequent detailed characterization studies.

The characterization of the synthesized nanoparticles included:

X-ray Diffraction (XRD): Conducted using a Bruker D8 Advance equipped with a Cu kα source to analyze cubic structure formation and determine nanoscale crystallite size. Scanning Electron Microscopy (SEM) with energy dispersive X-ray Analysis (EDAX): Utilized ZEISS, EVO LS15 equipment to examine nanoparticle morphology and composition. Transmission Electron Microscopy (TEM): Employed a Tecnai T20 microscope to further analyze the morphology and structure of the nanoparticles at higher resolution [47]. Fourier Transform Infrared Spectroscopy (FT-IR): Performed using a Thermo Scientific Nicolet iS10 to study chemical bonding and functional groups in the nanoparticles. Nitrogen physisorption in conjugation with Brunauer-Emmett-Teller (BET) and Barrett-Joyner-Halenda (BJT) analyses: Utilized Microtrac BELSORP-maxII to measure the surface area of the nanoparticles. Vibrating Sample Magnetometer (VSM): Employed a Lakeshore VSM 7407 to measure magnetic properties and characterize M-H loops. DC Resistivity Measurement: Used the two-probe technique to study electrical conductivity properties. Dielectric Measurements: Conducted using an LCR-Q meter Hioki 3532-50 to analyze the dielectric properties of the NPs.

3 Results and discussion

3.1 Structural studies

The structural analysis of the synthesized nanoparticles was conducted using X-ray diffraction (XRD) patterns, and Rietveld refinement was performed using FullProf software, as illustrated in Fig. 1(a–e). The superiority of the Rietveld refinement was validated through various parameters listed in Table 1. The XRD patterns in Fig. 1(a–e) exhibit distinct
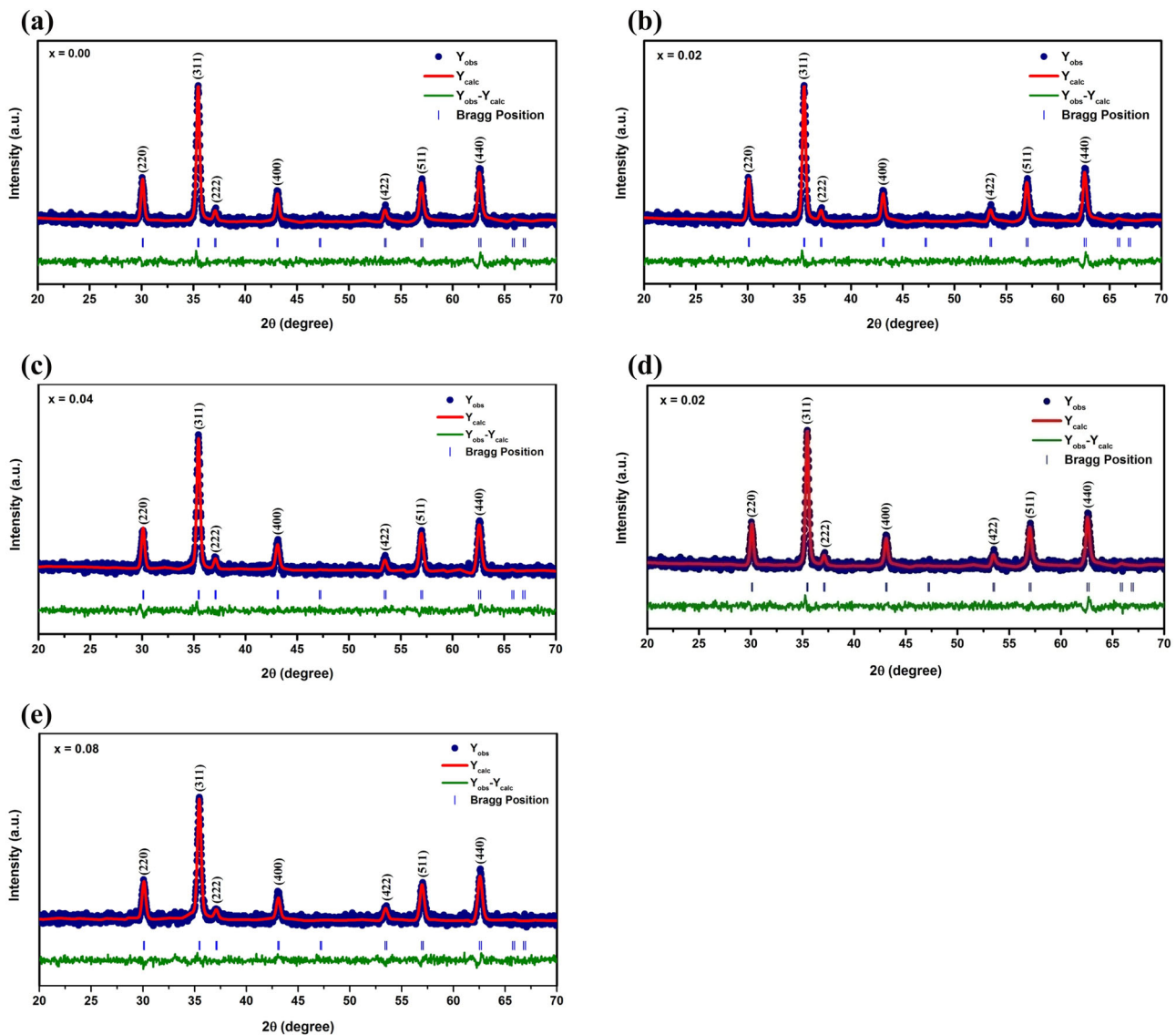
Fig. 1 **a** Rietveld refined XRD pattern of $CoFe_{2-2x}Al_xGd_xO_4$ ($x = 0.00$) nanoparticles. **b** Rietveld refined the XRD pattern of $CoFe_{2-2x}Al_xGd_xO_4$ ($x = 0.02$) nanoparticles. **c** Rietveld refined the XRD pattern of $CoFe_{2-2x}Al_xGd_xO_4$ ($x = 0.04$) nanoparticles. **d** Rietveld refined the XRD pattern of $CoFe_{2-2x}Al_xGd_xO_4$ ($x = 0.06$) nanoparticles. **e** Rietveld refined the XRD pattern of $CoFe_{2-2x}Al_xGd_xO_4$ ($x = 0.08$) nanoparticles

Table 1 Values of Rietveld refinement parameters: profile factor (R_p), weighted profile factor (R_{wp}), expected R-factor (R_{exp}), and goodness of fit (χ^2) for $CoFe_{2-2x}Al_xGd_xO_4$ ($x = 0.00, 0.02, 0.04, 0.06, 0.08$) nanoparticles

Composition (x)	R_p	R_{wp}	R_{exp}	χ^2
0.00	79.4	27.8	22.42	1.56
0.02	71.7	21.5	19.57	1.62
0.04	82.1	29.2	17.23	1.49
0.06	74.3	26.9	21.76	1.54
0.08	69.5	20.6	23.15	1.69

reflection planes indexed as '(220), (311), (222), (400), (422), (511), (440), (620), and (533)'. These reflections validate the occurrence of a single-phase face-centered cubic spinel structure. Each peak aligns well with previous research on cobalt ferrite nanoparticles indicating high structural integrity and phase purity without impurity peaks [48, 49]. Furthermore, the XRD results show a slight shift in Bragg's angle, suggesting successful co-doping of Al^{3+} and Gd^{3+} ions in the $CoFe_2O_4$ lattice (Fig. 1(a–e)). This shifting in the Bragg angles confirms the incorporation of Al^{3+} and Gd^{3+} ions into the crystal structure, validating the effectiveness of the co-doping process. The lattice constant was determined using [50],

$$a = d\sqrt{h^2 + k^2 + l^2}\,A, \tag{1}$$

where, d is the interplanar spacing, and h, k, l are the Miller indices.

Table 2 Values of calculated and theoretical lattice constant (a_{cal} and a_{th}), unit cell volume (V), X-ray density (d_X), bulk density (d_B), porosity (P), the average crystallite size (t) and dislocation density (δ) for $CoFe_{2-2x}Al_xGd_xO_4$ (x = 0.00, 0.02, 0.04, 0.06, 0.08) nanoparticles

Composition (x)	a_{cal} (Å)	a_{th} (Å)	V (Å³)	d_x (gm/cm³)	d_B (gm/cm³)	P (%)	t (nm)	$\delta \times 10^{-4}$ (nm⁻²)
0.00	8.382	8.381	588.9	5.292	3.552	32.9	23	19.39
0.02	8.385	8.383	589.5	5.336	3.567	32.2	21	21.73
0.04	8.389	8.387	590.4	5.361	3.604	32.8	21	23.66
0.06	8.392	8.390	591.0	5.388	3.661	32.1	20	24.65
0.08	8.396	8.397	591.9	5.429	3.692	32.0	19	26.41

Table 3 Values of ionic radii (r_A and r_B), hopping lengths (L_A and L_B), tetrahedral bond length (d_{AX}), octahedral bond length (d_{BX}), tetraedge shared (d_{AXE}), octaedge shared (d_{BXE}) and octaedge unshared (d_{BXEU}) for $CoFe_{2-2x}Al_xGd_xO_4$ (x = 0.00, 0.02, 0.04, 0.06, 0.08) nanoparticles

Composition (x)	r_A (Å)	r_B (Å)	L_A (Å)	L_B (Å)	d_{AX} (Å)	d_{BX} (Å)	d_{AXE} (Å)	d_{BXE} (Å)	d_{BEXU} (Å)
0.00	0.582	0.725	3.630	2.963	1.902	2.046	3.106	2.821	2.965
0.02	0.583	0.726	3.631	2.964	1.903	2.047	3.107	2.822	2.966
0.04	0.583	0.727	3.633	2.966	1.903	2.048	3.108	2.824	2.968
0.06	0.584	0.728	3.634	2.967	1.904	2.049	3.109	2.825	2.969
0.08	0.585	0.729	3.636	2.968	1.905	2.050	3.111	2.826	2.970

The lattice constant of the $CoFe_{2-2x}Al_xGd_xO_4$ nanoparticles ranged from 8.382 Å to 8.396 Å, showing an increasing trend with the co-doping, as detailed in Table 2. This variation in lattice constant is attributed to the substitution of Fe^{3+} ions (with a smaller ionic radius of 0.64 Å) by Gd^{3+} ions having larger ionic radii (0.94 Å). The lattice constant values were also estimated by Rietveld refinement analysis as shown in Table 2. The theoretical lattice constant values are in close agreement with the calculated lattice constant values from XRD data. The crystallite size (t) values were determined by [51],

$$t = \frac{0.9\lambda}{\beta \cos\theta} \text{nm} \quad (2)$$

where, λ is the wavelength, β is the full width at half maximum and θ is the angle.

The crystallite size of the $CoFe_{2-2x}Al_xGd_xO_4$ NPs ranged from 19 nm to 23 nm, exhibiting a decreasing trend with the co-doping, as detailed in Table 2. This variation indicates that the incorporation of Al^{3+} and Gd^{3+} ions influences the growth of crystallites in the nanoparticles. Furthermore, the observed crystallite sizes (19 nm to 23 nm) confirm the nanoscale behavior of the synthesized NPs. The dislocation density (δ) was calculated by [52],

$$\delta = \frac{1}{t^2} \text{lines/m}^2 \quad (3)$$

where, t is the crystallite size.

The dislocation density (δ) values varied between 19.39×10^{-4} lines/m² to 26.41×10^{-4} lines/m² as given in Table 2. The 'X-ray density values were determined by [52],

$$d_X = \frac{Z \times M}{V \times N_A} \text{gm/cm}^3 \quad (4)$$

where, Z is the coordination number, M is the molecular weight, V is the unit cell volume, and N_A is the Avogadro's number (6.022×10^{23}).

The X-ray density of the $CoFe_{2-2x}Al_xGd_xO_4$ NPs varied from 5.292 g/cm³ to 5.429 g/cm³, showing an increasing trend with the co-doping, as detailed in Table 2. This change in X-ray density reflects the alteration in the overall mass per unit volume due to the incorporation of larger Gd^{3+} ions into the crystal lattice compared to Fe^{3+} ions. Similarly, the bulk density values, determined using the Archimedes principle, ranged from 3.552 g/cm³ to 3.692 g/cm³, as indicated in Table 2. These values typically differ slightly from X-ray density due to factors such as porosity and the presence of air or other voids within the nanoparticle structure. The % porosity values were calculated by [53],

$$P = 1 - \frac{d_B}{d_X}\% \quad (5)$$

where, d_B is the bulk density and d_X is the X-ray density.

The % porosity varied between 31% to 33% with co-doping showing decreasing behavior as shown in Table 2. The hopping lengths L_A and L_B were determined by [53],

$$L_A = a\sqrt{3/4} \quad (6)$$

$$L_B = a\sqrt{2/4} \quad (7)$$

where, a is the lattice constant.

The hopping length values provided in Table 3 demonstrate an increase with higher levels of co-doping. This trend indicates that as the doping concentration of these ions increases, the hopping length within the crystal lattice also increases. The increase in hopping length can

Table 4 Values of interionic distances between cation-anion (p, q, r, and s) and cation-cation (b, c, d, e, and f) for $CoFe_{2-2x}Al_xGd_xO_4$ (x = 0.00, 0.02, 0.04, 0.06, 0.08) nanoparticles

Composition (x)	p (Å)	q (Å)	r (Å)	s (Å)	b (Å)	c (Å)	d (Å)	e (Å)	f (Å)
0.00	2.045	1.901	3.641	3.658	2.963	3.474	3.629	5.444	5.132
0.02	2.046	1.902	3.642	3.659	2.964	3.476	3.631	5.446	5.134
0.04	2.047	1.903	3.644	3.661	2.966	3.477	3.632	5.449	5.137
0.06	2.048	1.903	3.645	3.662	2.967	3.478	3.634	5.451	5.138
0.08	2.049	1.904	3.647	3.664	2.968	3.480	3.635	5.453	5.141

be directly linked to the expansion of the lattice parameter. The bond lengths were estimated using equation [50],

$$d_{AX} = a\sqrt{3\left(u - \frac{1}{4}\right)} \tag{8}$$

$$d_{BX} = a\sqrt{3u^2 - \frac{11}{4}u + \frac{43}{64}} \tag{9}$$

$$d_{AXE} = a\sqrt{2\left(2u - \frac{1}{2}\right)} \tag{10}$$

$$d_{BXE} = a\sqrt{2(1 - 2u)} \tag{11}$$

$$d_{BEU} = a\sqrt{4u^2 - 3u + \frac{11}{16}} \tag{12}$$

where u is the oxygen positional parameter.

The bond lengths reported in Table 3 exhibit an increase with the co-doping. This observation is consistent across all values, indicating that as the concentration of Al^{3+} and Gd^{3+} ions increases, the bond lengths within the $CoFe_{2-2x}Al_xGd_xO_4$ NPs also increase. The ionic radii (r_A and r_B) values were calculated using [52],

$$r_A = \left(u - \frac{1}{4}\right)a\sqrt{3} - r(O^{2-}) \tag{13}$$

$$r_B = \left(\frac{5}{8} - u\right)a - r(O^{2-}) \tag{14}$$

The values of ionic radii increase with the co-doping, as presented in Table 3. Considering the experimentally determined lattice constant and oxygen positional parameter (u = 0.381 Å), the interionic distances between cations (Me-Me: b, c, d, e, f) and between cations and anions (Me-O: p, q, r, s) were evaluated. These interionic distances play a crucial role in defining the predominant magnetic characteristics and are instrumental in elucidating the crystallographic structure. The interionic bond distances are calculated by following relations [50] and its values are

provided in Table 4.

$$p = a\left(\frac{5}{8} - u\right) \tag{15}$$

$$q = a\sqrt{3}\left(u - \frac{1}{4}\right) \tag{16}$$

$$r = a\sqrt{11}\left(u - \frac{1}{4}\right) \tag{17}$$

$$s = a\sqrt{3}\left(\frac{u}{3} + \frac{1}{8}\right) \tag{18}$$

$$b = \sqrt{2}\left(\frac{a}{4}\right) \tag{19}$$

$$c = \sqrt{11}\left(\frac{a}{8}\right) \tag{20}$$

$$d = \sqrt{3}\left(\frac{a}{4}\right) \tag{21}$$

$$e = \sqrt{3}\left(\frac{3a}{8}\right) \tag{22}$$

$$f = \sqrt{6}\left(\frac{a}{4}\right) \tag{23}$$

From Table 4, it is evident that interionic distances increase with the increase in co-doping. This observation implies that as the concentration of Al^{3+} and Gd^{3+} ions in the $CoFe_{2-2x}Al_xGd_xO_4$ NPs rises, both the Me-O (distances between cations and oxygen ions) and Me-Me (distances between cations) distances expand. The expansion of these interionic distances suggests a weakening of the interionic bonds within the crystal lattice. The bond angles were estimated using equations [52],

$$\theta_1 = Cos^{-1}\left(\frac{p^2 + q^2 - c^2}{2pq}\right) \tag{24}$$

$$\theta_2 = Cos^{-1}\left(\frac{p^2 + r^2 - e^2}{2pr}\right) \tag{25}$$

$$\theta_3 = Cos^{-1}\left(\frac{2p^2 - b^2}{2p^2}\right) \tag{26}$$

Table 5 Values of interionic angles (θ_1, θ_2, θ_3, θ_4 and θ_5) for CoFe$_{2-2x}$Al$_x$Gd$_x$O$_4$ (x = 0.00, 0.02, 0.04, 0.06, 0.08) nanoparticles

Composition (x)	θ_1 (degrees)	θ_2 (degrees)	θ_3 (degrees)	θ_4 (degrees)	θ_5 (degrees)
0.00	123.33	144.98	92.84	125.92	74.50
0.02	123.33	144.98	92.84	125.92	74.50
0.04	123.34	144.99	92.83	125.92	74.51
0.06	123.34	145.99	92.82	125.91	74.52
0.08	124.01	145.00	92.81	125.90	74.52

$$\theta_4 = Cos^{-1}\left(\frac{p^2 + s^2 - f^2}{2ps}\right) \qquad (27)$$

$$\theta_5 = Cos^{-1}\left(\frac{r^2 + q^2 - d^2}{2rq}\right) \qquad (28)$$

The calculated bond angles presented in Table 5 indicate specific trends i.e. θ_1, θ_2, and θ_5 increase, while θ_3 and θ_4 decrease with increasing co-doping. This variation in bond angles suggests structural modifications and changes in interatomic interactions within the crystal lattice.

3.2 Morphological and compositional studies

SEM images of typical samples of CoFe$_{2-2x}$Al$_x$Gd$_x$O$_4$ (x = 0.00 and 0.04) were examined to analyze their morphology, as depicted in Fig. 2. The images clearly show spherical-shaped nanoparticles with nanoscale grains. Additionally, some agglomeration is observed, likely due to interactions between the magnetic nanoparticles. The grain size was estimated using the linear intercept method, yielding values between 34 and 37 nm. These nanoscale grain sizes confirm the nanocrystalline nature of the samples, consistent with the findings from XRD analyses. The observed agglomeration suggests interactions between nanoparticles, which could further influence their collective magnetic behavior. The elemental composition of typical samples of CoFe$_{2-2x}$Al$_x$Gd$_x$O$_4$ (x = 0.00 and 0.04) was analyzed using energy dispersive X-ray analysis (EDAX), as illustrated in Fig. 3. The EDAX spectra exhibited excellent agreement between the measured elemental percentages and the expected weight and atomic percentages based on stoichiometry. The spectrum clearly shows the presence of Co, Fe, O, Al, and Gd, confirming the composition of CoFe$_{2-2x}$Al$_x$Gd$_x$O$_4$ nanoparticles. Importantly, the absence of any detectable traces of other metals in the EDAX spectrum indicates the high purity of the samples. The surface morphology and microstructure of typical samples of CoFe$_{2-2x}$Al$_x$Gd$_x$O$_4$ (x = 0.00 and 0.04) were investigated using transmission electron microscopy (TEM), as depicted in Fig. 4. The TEM images reveal spherical-shaped particles with noticeable agglomeration, likely caused by magnetic interactions among the particles. The average particle size estimated from TEM images are in between 19–22 nm. This nanometer-
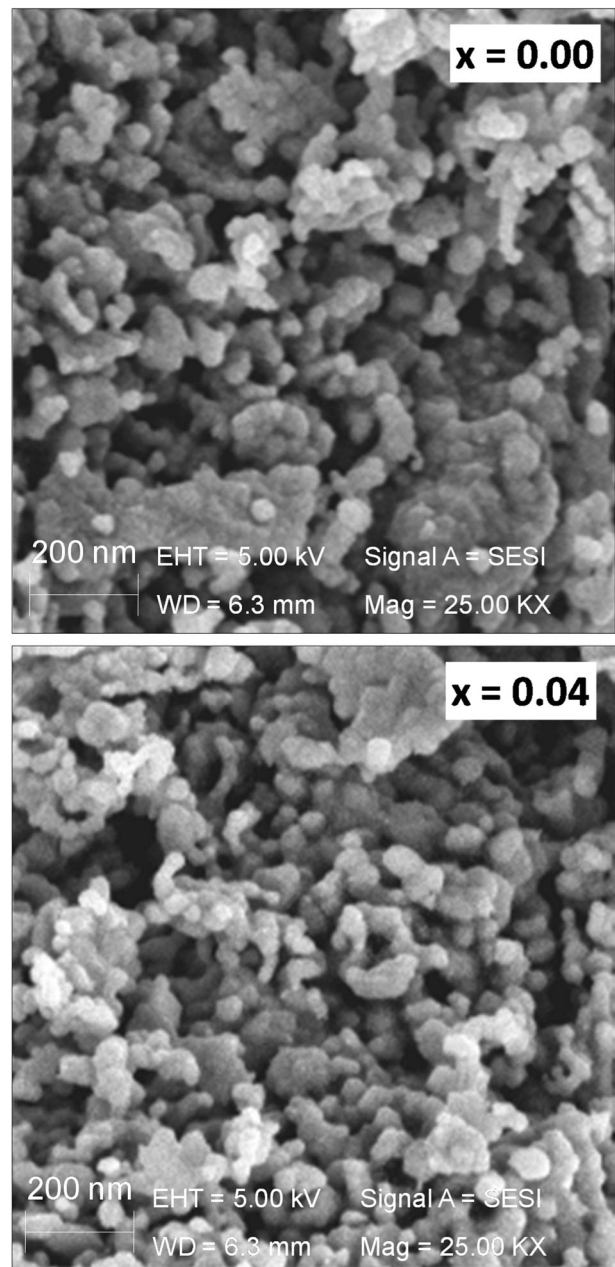
Fig. 2 FE-SEM images of typical samples of CoFe$_{2-2x}$Al$_x$Gd$_x$O$_4$ (x = 0.00 and 0.04)

scale particle size confirms the nanocrystalline nature of the prepared nanoparticles, which is consistent with the findings from XRD analysis. The observed agglomeration highlights the
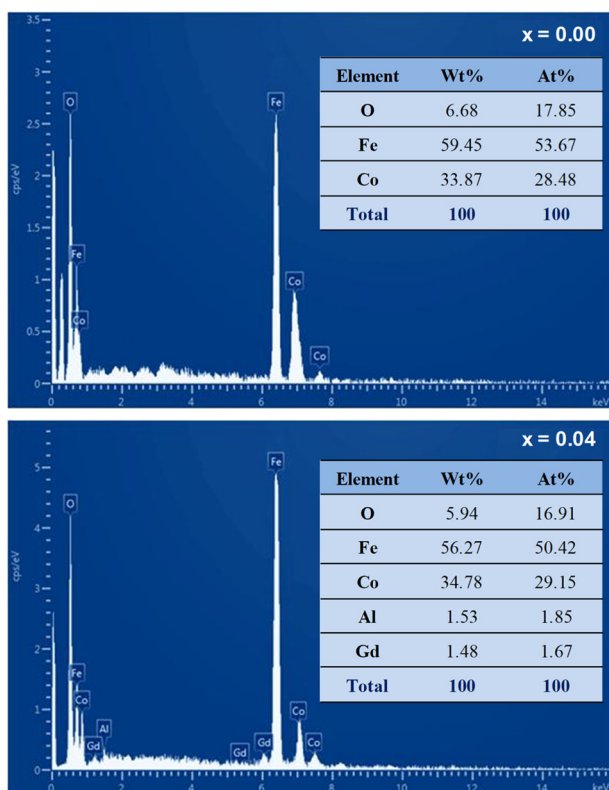
Fig. 3 EDAX spectra of typical samples of $CoFe_{2-2x}Al_xGd_xO_4$ (x = 0.00 and 0.04)

Fig. 4 TEM images of typical samples of $CoFe_{2-2x}Al_xGd_xO_4$ (x = 0.00 and 0.04)

magnetic interactions between nanoparticles, which can influence their collective magnetic behavior. The nanocrystalline behavior observed in TEM aligns well with XRD results, affirming the structural integrity and potential applications of these nanoparticles in various advanced technologies.

3.3 Infrared studies

The FT-IR spectra were recorded within the range of $380 \, cm^{-1}$ to $1000 \, cm^{-1}$, as illustrated in Fig. 5. The FT-IR spectra exhibit two distinct absorption bands around $600 \, cm^{-1}$ and $400 \, cm^{-1}$, characteristic of the spinel ferrite structure, specifically assigned to the tetrahedral (A) and octahedral (B) sites, respectively, within the spinel structure [54, 55]. The absorption wavenumber ν_1 and ν_2 are given in Table 6. It is observed from Table 6 that ν_1 shifts to higher wavenumber with co-doping. This shift occurs because as more Al^{3+} and Gd^{3+} ions are introduced, Fe^{3+} ions shift towards the oxygen ions at the (A) site, thereby reducing the Fe^{3+}-O^{2-} distance. This reduction leads to an increase in the ν_1 wavenumber. Conversely, ν_2 shifts to a lower wavenumber with co-doping. This shift is likely influenced by changes in the lattice dynamics or atomic interactions within the spinel structure as a result of dopant incorporation. The exact mechanism behind this shift requires further det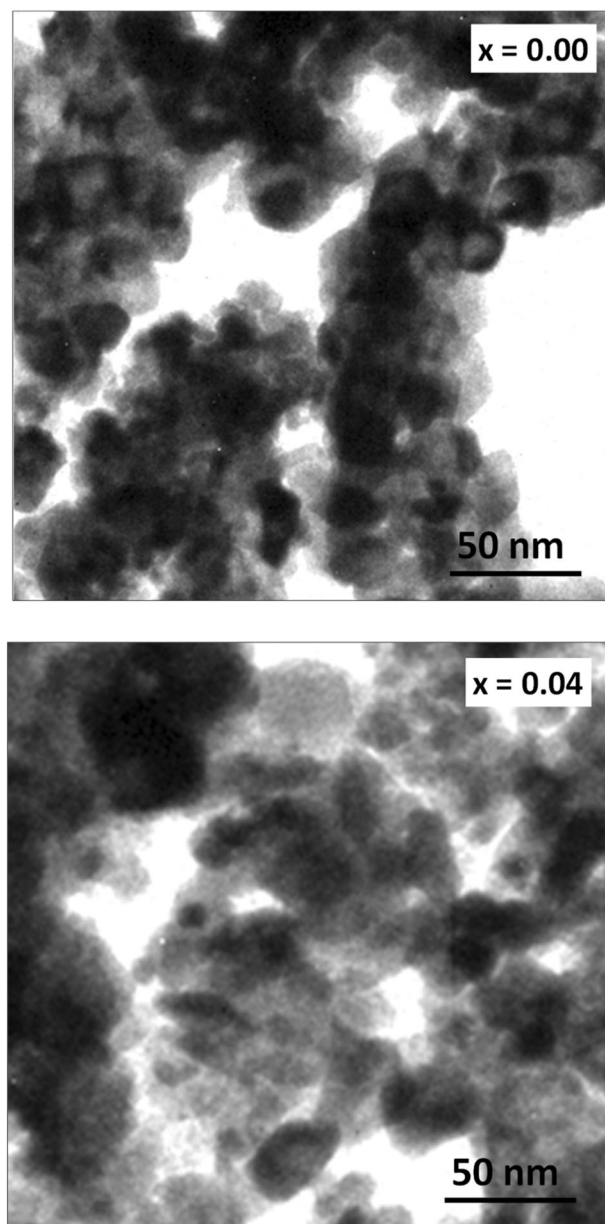ailed analysis, but it reflects the complex interplay between dopants and lattice vibrations. The force constants K_t and K_O (Table 6) were estimated by [50],

$$k_t = 7.62 \times M_1 \times \vartheta_1^2 \times 10^{-7} N/m \quad (29)$$

$$k_O = 10.62 \times M_2/2 \times \vartheta_2^2 \times 10^{-7} N/m \quad (30)$$

$$k_{av} = \frac{k_t + k_o}{2} \quad (31)$$

Here, the M_1 and M_2 are molecular weights of (A) and [B] site, respectively. It is observed that the K_O is smaller in comparison with the K_t.

3.4 Surface area studies

The physisorption of non-reactive gases, specifically nitrogen in this study, was employed to determine surface area and pore parameters. Nitrogen adsorption-desorption isotherms were recorded to analyze the textural characteristics, and the recorded isotherm curves for typical samples of $CoFe_{2-2x}Al_xGd_xO_4$ (x = 0.00, 0.04, and 0.08) NPs are depicted in Fig. 6(a–c). These isotherms exhibit a typical Langmuir type I-V isotherm with H3 hysteresis plots, characteristic of mesoporous materials. From the BET and BJH analyses, various surface parameters were derived and are detailed in Table 7. The BET surface area values ranged from 37 m^2/gm to 46 m^2/gm. It is notable from Table 7 that

the BET surface area increases with the co-doping. This increase suggests enhanced surface accessibility and adsorption capacity due to structural modifications induced by dopant incorporation. Furthermore, the average pore diameter and pore volume values also show an increase with increasing co-doping, as observed in Table 7. This indicates that the introduction of Al^{3+} and Gd^{3+} ions promotes the formation of larger pores within the nanoparticles, potentially enhancing their porosity and surface area. The observed increases in surface parameters with co-doping underscore the tunability of these nanoparticles for applications requiring specific surface properties, such as in catalysis, adsorption, and sensing technologies.

3.5 Magnetic studies

The M-H hysteresis loops displayed in Fig. 7 indicate a soft magnetic nature of all the samples. The magnetic parameters extracted from these loops are summarized in Table 8. It is observed from Table 8 that the saturation magnetization (M_s) decreases with co-doping, ranging from 49.18 emu/g to 65.23 emu/g. This decrease in M_s at higher concentrations of Al^{3+} and Gd^{3+} ions can be attributed to the substitution of magnetic Fe^{3+} ions by non-magnetic Al^{3+} and Gd^{3+} ions (which are non-magnetic at room temperature) within the crystal lattice [56, 57]. Additionally, the alteration of the exchange interactions between (A) and [B] sites may lead to either strengthening or weakening of the (B)-(B) and (A)-(B) interfaces, further influencing magnetization values [58, 59]. The decrease in M_s can also be accredited to the reduction in super-exchange interactions due to the co-doping of non-magnetic ions, thereby lowering the overall magnetization of the nanoparticles. Furthermore, the coercivity (H_c) of shows a decreasing trend with co-doping. The lowest H_c value observed was 74.81 Oe for the sample with x = 0.08. The values of magneton number (n_B) and magnetocrystalline anisotropy constant (K) was estimated by equations [60],

$$n_B = \left(\frac{Mol.Weight \times M_S}{5585} \right) \mu_B \tag{32}$$

$$K = \frac{H_C \times M_S}{0.96} \tag{33}$$

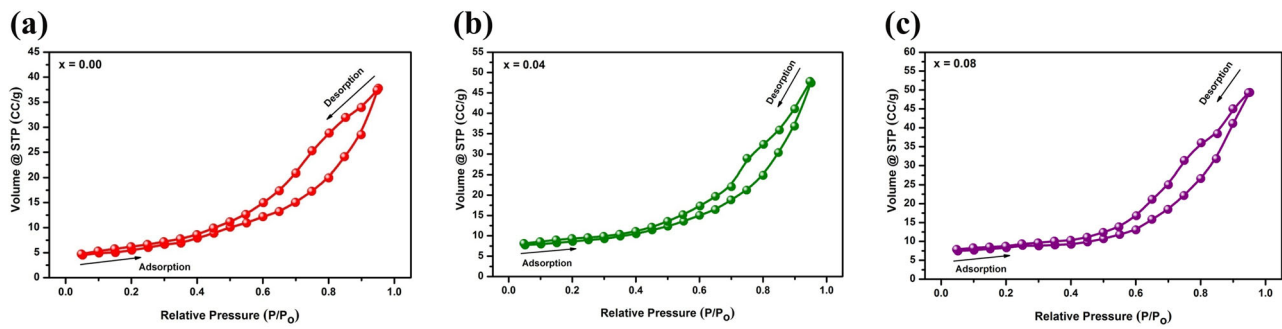where, M_S is the magnetization and H_C is the coercivity.

Fig. 5 FTIR spectrum of $CoFe_{2-2x}Al_xGd_xO_4$ (x = 0.00, 0.02, 0.04, 0.06, 0.08) nanoparticles

Table 6 Values of "infrared vibrational mode frequencies (ν_1 and ν_2) and Force constants (K_t, K_O, and K)" for $CoFe_{2-2x}Al_xGd_xO_4$ (x = 0.00, 0.02, 0.04, 0.06, 0.08) nanoparticles

Composition (x)	ν_1 (nm)	ν_2 (nm)	$K_t \times 10^2$ (N/m)	$K_O \times 10^2$ (N/m)	$K \times 10^2$ (N/m)
0.00	547	398	1.272	0.964	1.118
0.02	553	398	1.314	0.959	1.136
0.04	558	395	1.346	0.945	1.145
0.06	563	394	1.382	0.933	1.157
0.08	566	392	1.410	0.921	1.165

Fig. 6 a N_2 isotherm curve of a typical sample of $CoFe_{2-2x}Al_xGd_xO_4$ (x = 0.00). **b** N_2 isotherm curve of a typical sample of $CoFe_{2-2x}Al_xGd_xO_4$ (x = 0.04). **c** N_2 isotherm curve of typical sample of $CoFe_{2-2x}Al_xGd_xO_4$ (x = 0.08)

Table 7 Values of BET Surface area (S_{BET}), average pore diameter (P_D), and pore volume (P_V) for typical samples of $CoFe_{2-2x}Al_xGd_xO_4$ (x = 0.00, 0.02, 0.04, 0.06, 0.08)

Composition (x)	S_{BET} (m^2/gm)	P_D (nm)	P_V (cc/gm)
0.00	37	5.2	2.86
0.04	42	6.2	3.51
0.08	46	6.9	4.22
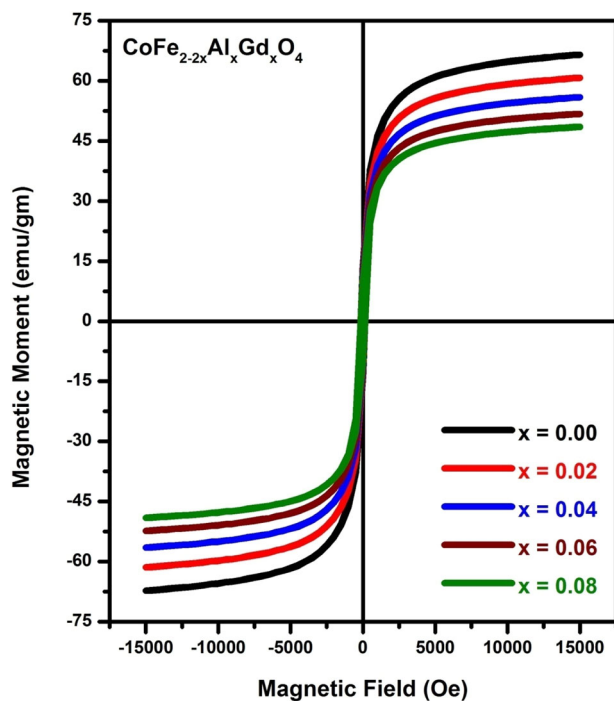
Fig. 7 M-H hysteresis plots of $CoFe_{2-2x}Al_xGd_xO_4$ (x = 0.00, 0.02, 0.04, 0.06, 0.08) nanoparticles

The value of the observed magneton number and magnetocrystalline anisotropy constant (K) are given in Table 8. The K values were found to be in the range of 3.83–12.11 K $\times 10^3$ (erg/Oe) and decreased with co-doping. The magnetization characteristics, including the remanence magnetization and the remanence ratio (M_r/M_S), exhibit behavior similar to the saturation magnetization upon co-doping. As indicated in Table 8, the M_r shows a decreasing trend with co-doping. The M_r/M_S values are noted to be lower than 0.5, indicating a multi-domain structure in the samples.

3.6 DC electrical resistivity analysis

The electrical properties of $CoFe_{2-2x}Al_xGd_xO_4$ (x = 0.00, 0.02, 0.04, 0.06, and 0.08) nanoparticles were analyzed by measuring DC electrical resistivity (DCR). The DCR can be obtained by [60],

$$\rho_{RT} = \frac{RA}{L} \qquad (34)$$

where, R = resistance, A = πr^2 and L = width of the pellet. Figure 8 depicts the changes in electrical resistivity (ρ) with the co-doping. The data clearly show a decrease in resistivity when these ions are introduced. One possible reason for this reduction is the decrease in the abundance of Fe^{3+} ions, which diminishes the likelihood of electron hopping between Fe^{3+} and Fe^{2+} ions [61, 62]. Additionally, nano-crystalline spinel ferrite is known to feature more grain boundaries, which act as barriers to electron movement, thereby reducing electrical resistivity. Factors such as grain boundaries, porosity, and stoichiometry significantly influence the material's resistivity by introducing additional insulating barriers. These factors collectively influence the material's electrical properties and are crucial considerations in optimizing its performance for various applications. Apart from grain boundaries, factors such as porosity and stoichiometry (the exact ratio of elements within the material) also play significant roles in determining the electrical resistivity of spinel ferrites. Higher porosity generally increases resistivity by introducing more insulating barriers. According to Verwey's model, electron conduction in spinel ferrite occurs via hopping among ions of the same element at octahedral [B] sites with different valency. Both Fe^{2+} and Fe^{3+} ions reside at these sites, facilitating electron conduction as electrons move between them.

Table 8 Values of saturation magnetization (M_S), remanence magnetization (M_r), coercivity (H_C), remanence ratio (M_r/M_S), magneton number (n_B) and anisotropy constant (K) for $CoFe_{2-2x}Al_xGd_xO_4$ (x = 0.00, 0.02, 0.04, 0.06, 0.08) nanoparticles

Composition (x)	M_S (emu/gm)	M_r (emu/gm)	H_C (Oe)	M_r/M_S	n_B (Obs.) (μ_B)	$K \times 10^3$ (erg/Oe)
0.00	65.23	18.21	178.24	0.279	2.74	12.11
0.02	59.82	16.55	155.71	0.277	2.54	9.70
0.04	55.95	15.34	119.36	0.274	2.39	6.95
0.06	52.06	14.06	95.37	0.270	2.23	5.17
0.08	49.18	12.97	74.81	0.264	2.13	3.83
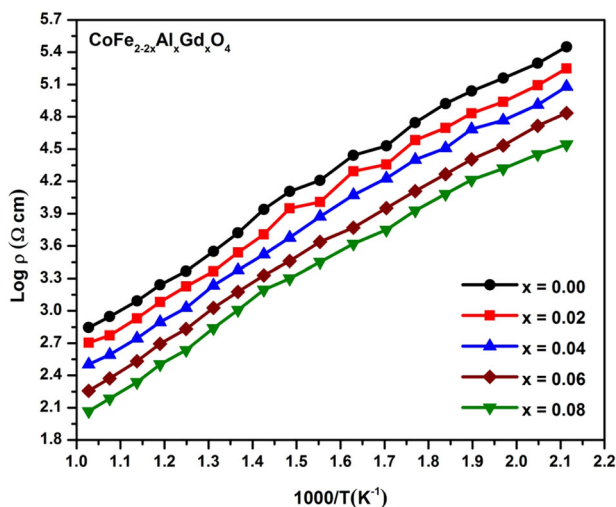
Fig. 8 DC resistivity plots of $CoFe_{2-2x}Al_xGd_xO_4$ (x = 0.00, 0.02, 0.04, 0.06, 0.08) nanoparticles
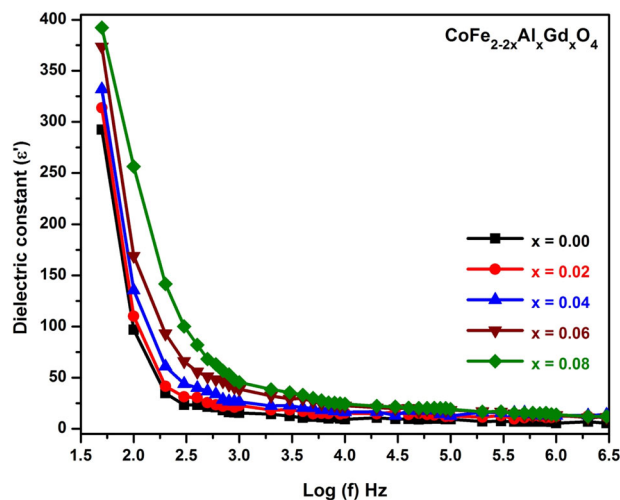
Fig. 9 Dielectric constant plots of $CoFe_{2-2x}Al_xGd_xO_4$ (x = 0.00, 0.02, 0.04, 0.06, 0.08) nanoparticles

3.7 Dielectric studies

The dielectric properties of all the samples were investigated by measuring the dielectric constant (ε'), dielectric loss (ε''), and dielectric loss tangent (tan δ) using an LCR-Q meter at room temperature across varying frequencies. Figure 9 illustrates the variation of dielectric constant with frequency. It reveals a consistent decrease in ε' as the frequency increases, indicating a frequency-independent trend across all samples. The dielectric parameters can be affected many parameters like particle sizes, structures, stoichiometric composition, and synthesis techniques [63, 64]. The noted decrease in ε' is related to the microstructure of the material. Ferrite materials typically consist of conducting grains separated by less conducting grain boundaries. At 'lower frequencies', the polarization behavior within the material, specifically space-charge polarization around non-ferroelectric regions adjacent to ferroelectric zones, contributes to the decrease in ε'. As the frequency increases, the electrical polarizability stabilizes, resulting in a more consistent ε' value at higher frequencies. The relationship between ε'', frequency, and tan δ is explored through Figs. 10 and 11 in the present study. Figure 10 illustrates that ε'' decreases exponentially as frequency increases. This decrease is similar to the behavior of ε', even though ε'' exhibits a more prominent decrease compared to ε'. The

tan δ, shown in Fig. 11, also demonstrates an exponential decrease with increasing frequency. The noted trend of tan δ can be attributed to Maxwell-Wagner interfacial polarization. This phenomenon arises due to variations in conductivity and dielectric constant within the material, particularly at interfaces between different phases or grains. Factors influencing tan δ include carrier concentration and structural uniformity. Furthermore, the study reveals that the dielectric parameters are influenced by the composition, specifically the co-doping. It is noted that increasing the concentration of these dopants enhances all dielectric characteristics. This compositional dependence underscores the importance of precise control over material composition in optimizing dielectric properties for various technological applications.

4 Conclusions

Trivalent Al^{3+} and Gd^{3+} ions were successfully co-doped into $CoFe_2O_4$ NPs with varying compositions represented as $CoFe_{2-2x}Al_xGd_xO_4$ (x = 0.00, 0.02, 0.04, 0.06, 0.08) using the sol-gel auto-combustion method. X-ray diffraction (XRD) analysis confirmed the formation of phase pure cubic spinel structures for all compositions. The lattice constant increased with Al^{3+} and Gd^{3+} ions co-doping due
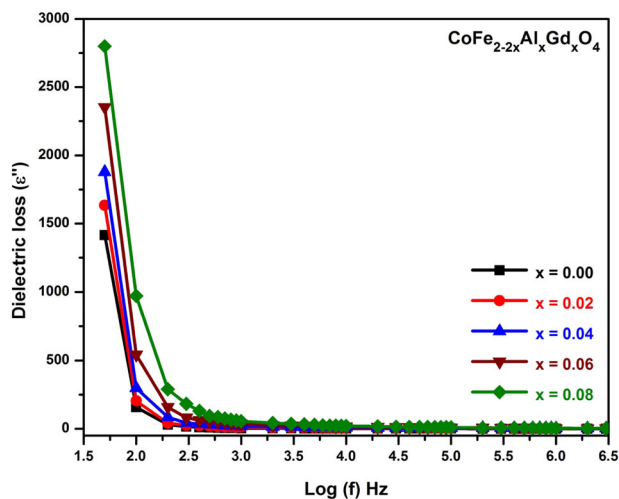
Fig. 10 Dielectric loss plots of $CoFe_{2-2x}Al_xGd_xO_4$ (x = 0.00, 0.02, 0.04, 0.06, 0.08) nanoparticles

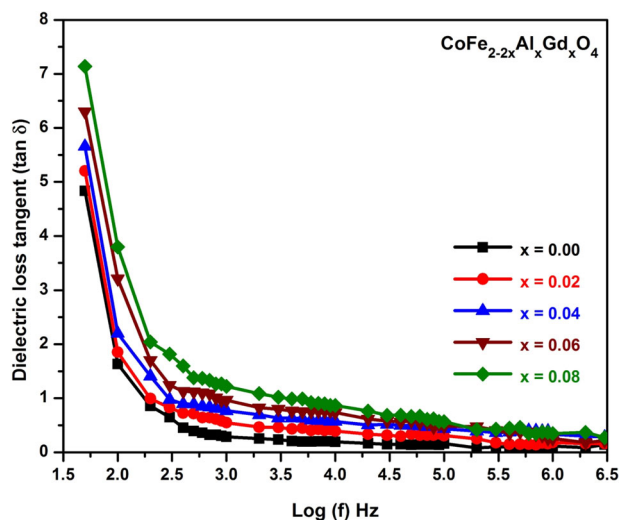**Fig. 11** Dielectric loss tangent plots of $CoFe_{2-2x}Al_xGd_xO_4$ (x = 0.00, 0.02, 0.04, 0.06, 0.08) nanoparticles

to the difference in ionic radii, highlighting the significant impact of co-doping on structural parameters. SEM imaging showed spherical grain shapes with some particle agglomeration, showing nanoscale characteristics. The average grain size corroborated the nanoscale nature of the particles. FTIR spectra revealed peaks corresponding to the cubic spinel ferrite structure. Magnetic properties showed a decrease in both saturation magnetization and magneton number with increasing Al^{3+} and Gd^{3+} ions co-doping levels. Conversely, the DC electrical resistivity decreased with higher co-doping levels, indicating improved electrical conductivity. Dielectric measurements exhibited a decrease in dielectric characteristics as frequency increased, a typical behavior in such materials. Overall, the co-doping of Al^{3+} and Gd^{3+} ions induced significant alterations in the features

of $CoFe_2O_4$ NPs. These modifications enhance their suitability for diverse applicability consisting high-frequency appliances, magnetic storage systems, biomedicine field, and beyond, showcasing their potential in advanced technological domains.

Data availability

The research data generated and analyzed during the current study are available from the corresponding author upon reasonable request.

Compliance with ethical standards

Conflict of interest The authors declare no competing interests.

Ethics This research study was conducted in compliance with ethical standards.

References

1. Wang S, Chen X, Luo K, Zhou H, Li R, He P, Paik K-W, Zhang S (2023) The design of low-temperature solder alloys and the comparison of mechanical performance of solder joints on ENIG and ENEPIG interface. J Mater Res Technol 27:5332–5339

2. Zhang Z, Chen J, Wang J, Han Y, Yu Z, Wang Q, Zhang P, Yang S(2022) Effects of solder thickness on interface behavior and nanoindentation characteristics in Cu/Sn/Cu microbumps. Welding in the World 66(5):973–983. https://doi.org/10.1007/s40194-022-01261-0

3. Lu B, Xia Y, Ren Y, Xie M, Zhou L, Vinai G, Morton SA, Wee AT, van der Wiel WG, Zhang W, Wong PKJ (2024) When Machine Learning Meets 2D Materials: A Review. Adv Sci 11(13):2305277. https://doi.org/10.1002/advs.202305277

4. Liu Q, Luo Y, Yang S, Xiong Y, Wang R, Fu X, Zhang R, Hu S, Bao X, Xu C (2023) Transfer-free in-situ synthesis of high-performance polybenzimidazole grafted graphene oxide-based proton exchange membrane for high-temperature proton exchange membrane fuel cells. J Power Sources 559:232666

5. Chen Y, Meng Y, Zhang J, Xie Y, Guo H, He M, Shi X, Mei Y, Sheng X, Xie D (2024) Leakage proof, flame-retardant, and electromagnetic shield wood morphology genetic composite phase change materials for solar thermal energy harvesting. Nano-Micro Lett 16:196

6. Yin S, Du Y, Liang X, Xie Y, Xie D, Mei Y (2023) Surface coating of biomass-modified black phosphorus enhances flame

retardancy of rigid polyurethane foam and its synergistic mechanism. Appl Surf Sci 637:157961

7. Wang J, Zhao Y, He C, Li K, Wang Z, Liu J, Zhang Q, Mao N, Cao Y (2024) Metal sulfides encapsulated in doped carbon aerogel towards superior and safe energy storage: two birds with one stone. Electrochim Acta 477:143819

8. Zhang X, Tang Y, Zhang F, Lee C-S (2016) A novel aluminum–graphite dual-ion battery. Adv Energy Mater 6:1502588

9. Yin C, Zhang T, Zhang C et al. Flexible mica films coated by magnetron sputtered insulating layers for high-temperature capacitive energy storage. SusMat. 2024;e228. https://doi.org/10.1002/sus2.228

10. Wang M, Jiang C, Zhang S, Song X, Tang Y, Cheng H-M (2018) Reversible calcium alloying enables a practical room-temperature rechargeable calcium-ion battery with a high discharge voltage. Nat Chem 10:667–672

11. X Guo, Q Peng, K Shin, Y Zheng, S Tunmee, C Zou, X Zhou, Y Tang Construction of a Composite Sn-DLC Artificial Protective Layer with Hierarchical Interfacial Coupling Based on Gradient Coating Technology Toward Robust Anodes for Zn Metal Batteries. Adv Energy Mater 2024, 2402015. https://doi.org/10.1002/aenm.202402015

12. Li L, Jia S, Yue S, Wang C, Qiu H, Ji Y, Cao M, Zhang D (2024) Hydrogel-stabilized zinc ion batteries: progress and outlook. Green Chem 26:6404–6422. https://doi.org/10.1039/D4GC01465K

13. Kuang W, Wang H, Li X, Zhang J, Zhou Q, Zhao Y (2018) Application of the thermodynamic extremal principle to diffusion-controlled phase transformations in Fe-CX alloys: Modeling and applications. Acta Mater 159:16–30

14. Xu X, Dong Y, Hu Q, Si N, Zhang C (2024) Electrochemical hydrogen storage materials: state-of-the-art and future perspectives. Energy Fuels 38:7579–7613

15. Chen Y, Guo Y, Xie B, Jin F, Ma L, Zhang H, Li Y, Chen X, Hou M, Gao J, Liu H, Lu Y-J, Wong C-P, Zhao N (2024) Lightweight and drift-free magnetically actuated millirobots via asymmetric laser-induced graphene. Nat Commun 15:4334

16. Mohammed L, Gomaa HG, Ragab D, Zhu J (2017) Magnetic nanoparticles for environmental and biomedical applications: A review. Particuology 30:1–14

17. Materón EM, Miyazaki CM, Carr O, Joshi N, Picciani PH, Dalmaschio CJ, Davis F, Shimizu FM (2021) Magnetic nanoparticles in biomedical applications: A review. Appl Surf Sci Adv 6:100163

18. Wang L, Wang G, Di Y, Wang H, Wang P, Dong L, Huang Y, Jin G (2024) Fast reversion of hydrophility-superhydrophobicity on textured metal surface by electron beam irradiation. Appl Surf Sci 669:160455. https://doi.org/10.1016/j.apsusc.2024.160455

19. Kefeni KK, Msagati TA, Mamba BB (2017) Ferrite nanoparticles: synthesis, characterisation and applications in electronic device. Mater Sci Eng: B 215:37–55

20. Akhlaghi N, Najafpour-Darzi G (2021) Manganese ferrite (MnFe2O4) Nanoparticles: From synthesis to application-A review. J Ind Eng Chem 103:292–304

21. Mathew DS, Juang R-S (2007) An overview of the structure and magnetism of spinel ferrite nanoparticles and their synthesis in microemulsions. Chem Eng J 129:51–65

22. Tatarchuk T, Bououdina M, Judith Vijaya J, John Kennedy L, Spinel ferrite nanoparticles: synthesis, crystal structure, properties, and perspective applications, In: Nanophysics, Nanomaterials, Interface Studies, and Applications: Selected Proceedings of the 4th International Conference Nanotechnology and Nanomaterials (NANO2016), August 24–27, 2016, Lviv, Ukraine, Springer, 2017, pp. 305–325

23. Srinivasan SY, Paknikar KM, Bodas D, Gajbhiye V (2018) Applications of cobalt ferrite nanoparticles in biomedical nanotechnology. Nanomedicine 13:1221–1238

24. Batoo KM, Hadi M, Chauhan A, Verma R, Singh M, Aldossary OM, Bhargava GK (2022) High-frequency applications of bismuth-doped Co–Zn ferrite nanoparticles for electromagnetic interference filter and multilayer inductor chip fabrication. Appl Phys A 128:283

25. Mokhosi SR, Mdlalose W, Nhlapo A, Singh M (2022) Advances in the synthesis and application of magnetic ferrite nanoparticles for cancer therapy. Pharmaceutics 14:937

26. Rao B, Shanmukhi P, Mammo TW, Kothandan D, Aregai T, Desta T, Kahsay M, Hagos G, Murali N, Batoo KM (2024) Investigation effect of Cr3+ substituted on enhanced dielectric and magnetic properties of co-cu nano ferrites for high-density data storage applications. Appl Phys A 130:1–14

27. Hadi M, Batoo KM, Chauhan A, Aldossary OM, Verma R, Yang Y (2021) Tuning of structural, dielectric, and electronic properties of Cu doped Co–Zn ferrite nanoparticles for multilayer inductor chip applications. Magnetochemistry 7:53

28. Qin H, He Y, Xu P, Huang D, Wang Z, Wang H, Wang Z, Zhao Y, Tian Q, Wang C (2021) Spinel ferrites (MFe2O4): Synthesis, improvement and catalytic application in environment and energy field. Adv Colloid Interface Sci 294:102486

29. Kiran A, Akhtar MN, Yousaf M, Batoo KM, Aldossary OM, Khan SN (2021) Influence of Y3+, Yb3+, Gd3+ cations on structural and electromagnetic properties of CuFe2O4 nanoferrites prepared via one step sol-gel method. J Rare Earths 39:1224–1231

30. Kefeni KK, Mamba BB, Msagati TA (2017) Application of spinel ferrite nanoparticles in water and wastewater treatment: a review. Sep Purif Technol 188:399–422

31. Srivastava R, Yadav BC (2012) Ferrite materials: introduction, synthesis techniques, and applications as sensors. Int J Green Nanotechnol 4:141–154

32. Sutka A, Mezinskis G (2012) Sol-gel auto-combustion synthesis of spinel-type ferrite nanomaterials. Front Mater Sci 6:128–141

33. Wani TA, Suresh G, Masrour R, Batoo KM, Rasool A (2023) A structural, morphological, optical and magnetic study of nickel-substituted zinc (Ni–Zn) ferrite nanoparticles synthesized via glycine assisted gel autocombustion synthesis route. Mater Chem Phys 307:128169

34. Jauhar S, Kaur J, Goyal A, Singhal S (2016) Tuning the properties of cobalt ferrite: a road towards diverse applications. RSC Adv 6:97694–97719

35. Mammo TW, Gebresilassie TA, Shanmukhi P, Teklehaimanot BT, Murali N, Batoo KM, Hussain S (2024) Study of structural, electrical and magnetic properties of co-substituted Co1− 2 x Ni x Mg x Fe2O4 (0≤ x≤ 0.25) nanoferrite materials. Appl Phys A 130:178

36. Mugutkar AB, Gore SK, Mane RS, Batoo KM, Adil SF, Jadhav SS (2018) Magneto-structural behaviour of Gd doped nanocrystalline Co-Zn ferrites governed by domain wall movement and spin rotations. Ceram Int 44:21675–21683

37. Batoo KM, Hadi M, Verma R, Chauhan A, Kumar R, Singh M, Aldossary OM (2022) Improved microwave absorption and EMI shielding properties of Ba-doped Co–Zn ferrite. Ceram Int 48:3328–3343

38. Kumar SR, Priya GV, Aruna B, Raju M, Parajuli D, Murali N, Verma R, Batoo KM, Kumar R, Narayana PL (2022) Influence of Nd3+ substituted Co0.5Ni0. 5Fe2O4 ferrite on structural, morphological, dc electrical resistivity and magnetic properties. Inorg Chem Commun 136:109132

39. Razia N, Shakeel K, Asokan K, Hilal A, Imran K (2012) Magnetic and electrical properties of In doped cobalt ferrite nanoparticles. J Appl Phys 112:084321. https://doi.org/10.1063/1.4759436

40. Köseoğlu Y, Alan F, Tan M, Yilgin R, Öztürk M (2012) Low temperature hydrothermal synthesis and characterization of Mn doped cobalt ferrite nanoparticles. Ceram Int 38:3625–3634

41. Karimi Z, Mohammadifar Y, Shokrollahi H, Asl SK, Yousefi G, Karimi L (2014) Magnetic and structural properties of nano sized

Dy-doped cobalt ferrite synthesized by co-precipitation. J Magn Magn Mater 361:150–156

42. Kalia R, Chauhan A, Verma R, Sharma M, Batoo KM, Kumar R, Hussain S, Ghotekar S, Ijaz MF (2022) Photocatalytic degradation properties of Li-Cr ions substituted CoFe2O4 nanoparticles for wastewater treatment application. Phys status solidi (a) 219:2100539

43. Kadam RH, Shitole R, Kadam SB, Desai K, Birajdar AP, Barote VK, Batoo KM, Hussain S, Shirsath SE (2023) A thorough investigation of rare-earth Dy3+ substituted cobalt-chromium ferrite and its magnetoelectric nanocomposite. Nanomaterials 13:1165

44. Kamran M, Anis-ur-Rehman M (2020) Enhanced transport properties in Ce doped cobalt ferrites nanoparticles for resistive RAM applications. J Alloy Compd 822:153583

45. Rather S-U, Bamufleh HS, Alhumade H (2021) Structural, thermal, morphological, surface, chemical, and magnetic analysis of Al3+-doped nanostructured mixed-spinel cobalt ferrites. Ceram Int 47:17361–17372

46. Jing X, Guo M, Li Z, Qin C, Chen Z, Li Z, Gong H (2023) Study on structure and magnetic properties of rare earth doped cobalt ferrite: The influence mechanism of different substitution positions. Ceram Int 49:14046–14056

47. Liu J, Xu J, Paik K-W, He P, Zhang S (2024) In-situ isothermal aging TEM analysis of a micro Cu/ENIG/Sn solder joint for flexible interconnects. J Mater Sci Technol 169:42–52

48. Singhal S, Barthwal S, Chandra K (2006) XRD, magnetic and Mössbauer spectral studies of nano size aluminum substituted cobalt ferrites (CoAlxFe2−xO4). J Magn Magn Mater 306:233–240

49. Raut VK, Somvanshi SB, Dawi EA, Birajdar CT (2024) Facile sol–gel synthesis of trivalent Al3+-Gd3+ ions co-doped nanoscale cobalt spinel ferrite for magneto-electronic applications. Inorg Chem Commun 168:112907

50. Somvanshi SB, Khedkar MV, Kharat PB, Jadhav K (2020) Influential diamagnetic magnesium (Mg2+) ion substitution in nano-spinel zinc ferrite (ZnFe2O4): thermal, structural, spectral, optical and physisorption analysis. Ceram Int 46:8640–8650

51. Jadhav SA, Khedkar MV, Somvanshi SB, Jadhav K (2021) Magnetically retrievable nanoscale nickel ferrites: an active photocatalyst for toxic dye removal applications. Ceram Int 47:28623–28633

52. Somvanshi SB, Jadhav SA, Khedkar MV, Kharat PB, More S, Jadhav K (2020) Structural, thermal, spectral, optical and surface analysis of rare earth metal ion (Gd3+) doped mixed Zn–Mg nano-spinel ferrites. Ceram Int 46:13170–13179

53. Bharati V, Somvanshi SB, Humbe AV, Murumkar V, Sondur V, Jadhav K (2020) Influence of trivalent Al–Cr co-substitution on the structural, morphological and Mössbauer properties of nickel ferrite nanoparticles. J Alloy Compd 821:153501

54. Hutamaningtyas E, Wijayanta A, Purnama B, FTIR and structural properties of co-precipitated cobalt ferrite nano particles. In: J Phys: Conference Series, IOP Publishing, 2016, pp. 012023.

55. Kharat PB, Somvanshi SB, Dawi EA, Mopari AM, Bansod NH (2024) Exploring the electrochemical performance of nickel-zinc ferrite nanoparticles for supercapacitor applications. J Mater Sci: Mater Electron 35:606

56. Ansari S, Arabi H, Alavi Sadr SM (2016) Structural, morphological, optical and magnetic properties of Al-doped CoFe2O4 nanoparticles prepared by Sol-Gel auto-combustion method. J Superconduct Nov Magn 29:1525–1532

57. Kharat PB, Somvanshi SB, Somwanshi SB, Mopari AM, Low-cost fabrication of Zn-doped MnFe2O4 (Mn0.5Zn0.5Fe2O4) film for H2S gas sensing applications. In: Macromolecular Symposia, Wiley Online Library, 2021, pp. 2100147

58. Dipesh DN, Wang L, Adhikari H, Alam J, Mishra S (2016) Influence of Al3+ doping on structural and magnetic properties of CoFe2-xAlxO4 Ferrite nanoparticles. J Alloy Compd 688:413–421

59. Kharat PB, Somvanshi SB, Somwanshi SB, Mopari AM, Investigation of super-capacitive properties of nanocrystalline copper-zinc (Cu0.5Zn0.5Fe2O4) ferrite nanoparticles, In: Macromolecular Symposia, Wiley Online Library, 2021, pp. 2100162

60. Bhosale AB, Somvanshi SB, Murumkar V, Jadhav K (2020) Influential incorporation of RE metal ion (Dy3+) in yttrium iron garnet (YIG) nanoparticles: magnetic, electrical and dielectric behaviour. Ceram Int 46:15372–15378

61. Priya AS, Geetha D, Kavitha N (2019) Effect of Al substitution on the structural, electric and impedance behavior of cobalt ferrite. Vacuum 160:453–460

62. Gul I, Maqsood A (2008) Structural, magnetic and electrical properties of cobalt ferrites prepared by the sol–gel route. J Alloy Compd 465:227–231

63. Anukool W, El-Nabulsi RA, Dabagh S (2023) Effect of Al3+ doping on dielectric properties of cobalt ferrite nanoparticle for using in high frequency applications,. J Sol-Gel Sci Technol 105:405–415

64. Priya AS, Geetha D, Kavitha N (2018) Evaluation of structural and dielectric properties of Al. Ce co-doped cobalt ferrites, Mater Res Express 5:066109